



## Laboratory characterisations and intercomparison sounding test of dual thermistor radiosondes for radiation correction

Sang-Wook Lee<sup>1,2</sup>, Sunghun Kim<sup>1</sup>, Young-Suk Lee<sup>1</sup>, Jae-Keun Yoo<sup>1</sup>, Sungjun Lee<sup>1</sup>, Suyong Kwon<sup>1,2</sup>,  
Byung Il Choi<sup>1</sup>, Jaewon So<sup>3</sup>, Yong-Gyoo Kim<sup>1,\*</sup>

5 <sup>1</sup>Division of Physical Metrology, Korea Research Institute of Standards and Science, Daejeon 34113, Republic of Korea

<sup>2</sup>Department of Science of Measurement, University of Science and Technology, Daejeon 34113, Republic of Korea

<sup>3</sup>Weather, Gunpo 15880, Republic of Korea

\*Correspondence to: Y.-G. Kim ([dragon@kriss.re.kr](mailto:dragon@kriss.re.kr))

**Abstract.** A dual thermistor radiosonde (DTR) comprising two (white and black) sensors with different emissivities was  
10 developed to correct the effects of solar radiation on temperature sensors based on *in-situ* radiation measurements. Herein,  
the DTR performance is characterised in terms of the uncertainty via a series of ground-based facilities and an  
intercomparison sounding test. The DTR characterisation procedure using laboratory facilities is as follows: individually  
calibrate the temperature of the thermistors in a climate chamber; test the effect of temperature on the resistance reading  
using radiosonde boards in the climate chamber; individually perform radiation tests on thermistors; and perform  
15 parameterisation of the radiation measurement and correction formulas using an upper air simulator with varying  
temperature, pressure and ventilation speed. These results are combined and applied to the DTR sounding test conducted in  
July, 2021. Thereafter, the effective irradiance is measured using the temperature difference between the white and black  
sensors of the DTR. The measured irradiance is then used for the radiation correction of the DTR white sensor. The  
radiation-corrected temperature of the DTR is mostly consistent with that of a commercial radiosonde (Vaisala, RS41)  
20 within the expanded uncertainty ( $\sim 0.35$  °C) of the DTR at the coverage factor  $k = 2$ . Furthermore, the components  
contributing to the uncertainty of the radiation measurement and correction are analysed. The DTR methodology can  
improve the accuracy of temperature measurement in the upper air within the framework of the traceability to the  
International System of Units.



## 25 1 Introduction

Measurement of environmental parameters such as temperature and water vapour (i.e. humidity) is important as they are essential input data for weather and climate prediction models (Bojinski et al., 2014). The temperature and humidity in upper air are frequently and widely measured using radiosondes. Radiosonde is a telemetry device comprising various sensors that measure environmental parameters and transmit the measurement data via radio frequency while being flown by a weather balloon up to about 35 km in altitude. Radiosonde measurements are known to be more accurate than measurement methods based on remote sensing techniques, such as LIDAR and satellite. Thus, radiosonde measurements are often used as reference to correct other measurement data. Hence, the measurement accuracy of radiosondes needs to be improved in terms of uncertainty within the framework of the traceability to the International System of Units (SI).

Joint research programs between the metrology and the meteorology and climate communities, such as the ‘MeteoMet– Metrology for Meteorology’ project, were initiated (Merlone et al., 2015; Merlone et al., 2018) to acquire high quality observation data on meteorological variables. Reference facilities have been developed through the project for calibrating the meteorological observation instruments to be used in the meteorological community, such as the Global Climate Observing System (GCOS). Additionally, low-temperature and low-pressure humidity chambers have been developed for calibrating radiosonde humidity sensors when the project deliverables were limited to the field of upper air measurement by radiosondes (Sairanen et al., 2015; Cuccaro et al., 2018). To resolve the long-term climate change, a certain amount of measurement uncertainty of radiosonde sensors is required for actual soundings in addition to the ground-based facilities. Hence, the GCOS Reference Upper Air Network (GRUAN) was founded to establish the highest level of quality control in the upper air measurement in terms of uncertainty (Gcos, 2007). The measurement accuracy of temperature specified by GRUAN is 0.2 °C in the stratosphere (Gcos, 2007).

A difficulty in improving the measurement accuracy of radiosondes is the compensation of the solar-radiation-induced heating of sensors during the daytime. The radiative heating of sensors is also affected by environmental conditions, such as temperature, air pressure and air ventilation, that are involved with convective cooling (Lee et al., 2018b; Lee et al., 2020). All these parameters should be considered together to precisely evaluate the radiation correction of radiosonde temperature sensors. Although most radiosonde manufacturers apply radiation corrections to their products (Nash et al., 2011), they do not disclose the detailed methodologies, including reference systems and correction algorithms. Thus, the uncertainty evaluation on the radiation correction by manufacturers cannot be fully accepted. To independently evaluate the radiosondes, GRUAN has built a ground-based calibration facility and established a correction algorithm for the GRUAN data processing (GDP) of the Vaisala RS92 radiosonde (Dirksen et al., 2014). Recently, the same group built a new simulator to investigate the solar temperature error of radiosondes (SISTER) and derived a new GDP algorithm for the Vaisala RS41 radiosonde (Von Rohden et al., 2021). The setup can control the irradiance, air pressure, ventilation, sensor rotation and tilting of the light incident angle. However, the surrounding temperature, which also affects the radiation correction, cannot be changed, as previously reported (Lee et al., 2018a). Furthermore, an upper-air simulator (UAS) was developed by the Korea research



institute of standards and science (KRISS) to similarly evaluate radiosondes (Lee et al., 2020). The UAS at KRISS can simultaneously control the temperature, pressure, ventilation and irradiance, and the UAS was recently supplemented with sensor tilting and rotation functions. Using this setup, a radiation-correction formula of the RS41 radiosonde is presented independent of the manufacturers (Lee et al., 2021).

However, the radiation correction processes by GRUAN and KRISS assume that the solar irradiance is known. In fact, the solar irradiance is dependent on various parameters such as cloud conditions, solar elevation angle, season and location. Till date, the direct *in-situ* measurements of solar irradiance are difficult without using additional pyranometers during soundings (Philipona et al., 2013). An alternative approach comprises the simulation of solar irradiance with appropriate cloud scenarios, surface albedo and solar angle (Key and Schweiger, 1998). From the perspective of the radiation correction uncertainty, the SI traceability of the simulated irradiance is incomplete and may increase the radiation correction uncertainty.

To resolve this issue, the concept of a dual thermistor radiosonde (DTR) comprising two temperature sensors with difference emissivities was introduced to measure the effective irradiance using the temperature difference between them (Lee et al., 2018a; Lee et al., 2018b). The DTR operation principle was demonstrated by investigating the effects of air ventilation and temperature and pressure using a wind tunnel and a freezing chamber system, respectively. The temperature difference between the dual thermistors was linearly proportional to the effective irradiance, and the radiation-induced heating of the sensors was corrected according to the measured effective irradiance. Only the slope of the linear function of the radiation measurements and correction formulas changed with the environmental parameters, and the linearity itself was not altered. However, these DTR formulas were obtained using two separate setups that cannot be combined, and thus, the correction formula was incomplete in terms of the SI traceability.

Herein, the combined effect of temperature, pressure, ventilation and irradiance on DTR is investigated using the UAS at KRISS for the parameterisation of the radiation measurements and correction formulas. The obtained formulas were used in an intercomparison sounding test that was performed in July, 2021. Furthermore, a series of laboratory characterisations of DTR is conducted, including individual calibration of thermistors, test of temperature effect on resistance reading by radiosonde boards and individual radiation test on thermistors. The uncertainties due to parameterisation of the radiation correction formula using UAS and other characterisations are also evaluated. Then, the uncertainty components and their combined budget for the measured irradiance and corrected temperature in the sounding test are presented. Finally, the difference between the corrected temperatures of DTR and the RS41 radiosonde is presented with the DTR uncertainty.

## 2 Introduction to DTR

### 2.1 Dual thermistors with different emissivity

Figure 1(a) shows a DTR comprising two temperature sensors that are chip-in-glass type negative temperature coefficient (NTC) thermistors (Shibaura electronics, Model: PB7-41E). The glass bead encapsulating the sensing element is ellipsoidal



90 shape with 0.55 mm diameter and 1.1 mm length. The two thermistors are attached to the sensor boom via soldering and followed by epoxy for electrical insulation. The thermistors and sensor boom are coated with aluminium (Al) via thermal evaporation. One sensor is additionally coated with a black epoxy (Loctite, Model: STYCAST 2850 FT) to differentiate the emissivity (absorptivity) between them (inset of Fig. 1(a)). For convenience, herein, the sensor coated with only Al is referred to as the white sensor, while the other sensor is referred to as the black sensor.

## 95 2.2 DTR operation principle

DTR utilises the temperature difference between the white and black sensors to measure the effective irradiance and correct its effect on the white sensor (Fig. 1(b)). The temperature increase of each sensor due to solar irradiation is linearly proportional to the effective irradiance, as previously investigated by various theoretical and experimental studies (Lee et al., 2018b; Lee et al., 2018a; Luers, 1990; Mcmillin et al., 1992). Additionally, the temperature of the black sensor ( $T_{B\_raw}$ ) is higher than that of the white sensor ( $T_{W\_raw}$ ) due to its high light absorptivity. Thus, the temperature difference between them ( $T_{B\_raw} - T_{W\_raw}$ ) is also linearly proportional to the effective irradiance. Although other environmental parameters, e.g. air pressure and ventilation, affect the degree of heating of sensors via convective cooling; they only change the slope of the linear function and do not affect the linearity itself. The effect of other environmental parameters on the temperature difference and the temperature increase of the white sensor are investigated using the UAS developed at KRISS. Experimental results of the UAS are used to determine a formula to measure the effective irradiance based on the temperature difference between the two thermistors. Then, the effective irradiance and other environmental factors are parameterised into a single equation to calculate the radiation correction of the white sensor ( $T_{W\_raw} - T_{W\_cor}$ ). Section 4 describes the procedure to obtain these formulas for the measurement of irradiance and the correction of the white sensor using the UAS in more detail.

## 110 3 DTR characterisation

### 3.1 Characterisation procedure

The DTR characterisation procedure is summarised in Figures 2(a)–(e). The characterisation process is categorised into laboratory experiments and sounding test. First, the thermistors on the sensor boom are individually calibrated using a climate chamber (Fig. 2(a)). Then, the temperature effect on the resistance reading by radiosonde boards is tested in the climate chamber (Fig. 2(b)). The temperature increase of all thermistors via irradiation is individually recorded at room temperature (Fig. 2(c)) to compensate for the difference among units for radiation correction. The radiation measurement and correction formulas of DTR are obtained using the UAS with varying temperature, pressure, ventilation speed and irradiance (Fig. 2(d)). The laboratory experimental results are combined and applied to the DTR sounding system. Then, the sounding results of DTR are compared with those of a commercial radiosonde through dual soundings (Fig. 2(e)).



### 120 3.2 Individual calibration of thermistors in a climate chamber

All thermistors are individually calibrated in a climate chamber (Kambic, Model: KK-190 CHULT). Figure 3(a) displays the calibration setup showing the sensors on the booms in the climate chamber, a digital multimeter (Keysight, Model: 34980A) to record the sensor resistances and a data acquisition computer. The setup can calibrate 35 pairs ( $7 \times 5$ ) of dual thermistors that are located on the same rectangular plane (230 mm  $\times$  190 mm). Five platinum resistance thermometers (PRT) with a  
125 nominal resistance of 100  $\Omega$  (PT100) are used as reference thermometers. They were calibrated at KRISS with an uncertainty of 0.05  $^{\circ}\text{C}$  at a coverage factor  $k = 2$  and installed at the centre and four corners in the same rectangular plane as the thermistors. The average of the temperatures measured by five reference PRTs ( $T_{\text{Ref\_aver}}$ ) is used as the reference temperature for calibration. Six calibration points are selected from  $-70$  to 30  $^{\circ}\text{C}$  (Fig. 3(b)), of which y-axis denotes the spatial temperature gradient ( $T_{\text{Ref\_grad}}$ ) represented by the maximum deviation from  $T_{\text{Ref\_aver}}$ .

130 Generally, the Steinhart–Hart equation is used for the calibration of NTC thermistors (White, 2017). However, the application of a third-order polynomial equation yields smaller fitting residuals than that of a second-order equation (not shown here). Therefore, the former equation is adopted for the calibration as follows:

$$\frac{1}{T_S} = a_0 + a_1 \ln(R_S) + a_2 [\ln(R_S)]^2 + a_3 [\ln(R_S)]^3, \quad (1)$$

where  $T_S$  is the sensor temperature obtained based on the sensor resistance  $R_S$  and  $a_0$ ,  $a_1$ ,  $a_2$  and  $a_3$  are the fitting coefficients.  
135 The distributions of the fitting residuals of the white and black sensors are shown in Figs. 3(c) and (d), respectively. Totally, 696 data points are obtained, collected from six calibration points of 116 thermistors of the same colour. No essential difference is observed between the white and black sensors in the distributions of the residuals, implying that the emissivity difference plays a negligible role in the sensor calibration process.

Furthermore, the uncertainty of radiosonde sensors due to calibration  $U(T_{S\_cal})$  at  $k = 2$  is calculated, as shown in Fig. 3(e).  
140 The contributing uncertainty factors are temperature gradient  $U(T_{\text{Ref\_grad}})$ , stability  $U(T_{\text{Ref\_stab}})$  and calibration  $U(T_{\text{Ref\_cal}})$  of the reference PRTs and the temperature stability  $U(T_{S\_stab})$  and fitting residuals  $U(T_{S\_fit\_resid})$  of the sensors. Consequently, the uncertainty of thermistors due to calibration is about 0.1–0.3  $^{\circ}\text{C}$  ( $k = 2$ ) between 30 and  $-70$   $^{\circ}\text{C}$ .

### 3.3 Test of temperature effect on resistance reading by radiosonde boards

To measure the temperature using the thermistors via Eq. (1), the measurement of the sensor resistance by the radiosonde  
145 boards should be evaluated in the temperature range of the sensor calibration. Thus, ten radiosonde prototypes covered with expanded polystyrene foam are installed in the climate chamber with varying temperatures. The radiosonde boards are wired to external reference resistors (Cropico, Model: 008-B) instead of thermistors, as shown in Fig. 4(a). The resistance measured by radiosonde boards is collected by a computer via wired communication.

Figure 4(b) shows the difference between the reference resistance and radiosonde reading as a function of the reference  
150 resistance. The reference resistance is changed according to the environmental temperature of the radiosonde boards, which



is varied from  $-70$  to  $20$  °C. For example, a reference resistance of  $700$  k $\Omega$  is chosen to imitate the sensor resistance of  $-70$  °C when the temperature of the climate chamber measured by reference PRTs ( $T_{\text{Ref\_aver}}$ ) is  $-70$  °C. Thereafter, both the reference resistance and resistance reading by radiosonde boards are converted into temperatures using a calibration curve based on Eq. (1). The resultant temperature error by radiosonde boards with varying temperature is shown in Fig. 4(c). Since the temperature error is roughly distributed within  $\pm 0.05$  °C, the standard deviation of all data points is obtained ( $0.04$  °C) and is used for uncertainty ( $k = 1$ ) due to the influence of temperature on the resistance reading by radiosonde boards.

### 3.4 Individual radiation test on radiosonde thermistors

A difficulty faced during the radiation correction of these thermistors is the unit difference in terms of the correction value. This can be attributed to the irregularity in the thermistor glass bead sizes, the black epoxy coating and the sensor connection to the boom via soldering and epoxy. Effective irradiance to thermistors and the cooling by convection can be changed based on the glass bead sizes and the Al and black epoxy coatings. The irregular connection between the sensor and boom may affect the thermal conduction between them. However, obtaining radiation correction formulas of radiosondes individually using UAS with varying temperature, pressure, air ventilation speed and irradiance is time-consuming and economically unfavourable. Therefore, a radiation test is performed on all thermistors in a vacuum chamber at room temperature ( $\sim 25$  °C), and the results are correlated to the UAS experiments to acquire sensor-specific radiation correction formulas that reflect the unit difference.

Figure 5(a) shows an individual radiation test setup comprising a solar simulator, vacuum pump, vacuum chamber, digital multimeter and computer. A pair of dual thermistors is illuminated through a window in the lid of the vacuum chamber. The rotation of 12 pairs of sensors and the light irradiation of the solar simulator are automatically controlled using a computer program. When a pair of dual thermistors arrives and stops beneath the window during rotation, the window is screened by a shutter to block the light irradiation. At this time, the irradiance is measured using a calibrated pyranometer on the shutter. Then, the shutter is opened and a pair of thermistors are illuminated for 180 s. Temperatures of the white ( $T_{\text{W}}$ ) and black ( $T_{\text{B}}$ ) sensors are recorded (Fig. 5(b)), and 107 pairs of dual thermistors are tested in total. Figures 5(c) and (d) show the temperature difference distributions between a pair of thermistors ( $T_{\text{B\_on}} - T_{\text{W\_on}}$ ) and the temperature increase of the white sensor ( $T_{\text{W\_on}} - T_{\text{W\_off}}$ ), respectively. The subscript on and off indicate when the light irradiation is turned on and off, respectively. These values are used as parameters for the sensor-specific radiation correction formulas obtained by UAS experiments. Five representative pairs of thermistors are selected for the radiation correction experiments using UAS, as indicated by black arrows in Figs. 5(c) and (d).



#### 4 Parameterisation for radiation measurement and correction by DTR using UAS

##### 180 4.1 Radiation measurement by DTR

Figures 6(a)–(e) show the UAS measurements for five representative temperature differences ( $T_{B\_on} - T_{W\_on}$ ) between a pair of dual thermistors selected from the rotational radiation test (RRT) in Fig. 5(c). A previous study reported that UAS has the capability of simultaneously varying environmental parameters for the radiation correction of commercial radiosondes (Lee et al., 2020). In Fig. 6, air pressure ( $P$ ) is varied from 5 to 500 hPa and temperature ( $T_{W\_on}$ ) is varied from  $-68$  to  $20$  °C with a fixed irradiance ( $S_0 = 960 \text{ W} \cdot \text{m}^{-2}$ ) and ventilation speed ( $v_0 = 5 \text{ m} \cdot \text{s}^{-1}$ ). As expected, the level of  $(T_{B\_on} - T_{W\_on})_{\text{RRT}}$  is positively correlated with the degree of  $(T_{B\_on} - T_{W\_on})_{\text{UAS}}$ , exhibiting a gradual decrease of  $(T_{B\_on} - T_{W\_on})_{\text{UAS}}$  with decreasing  $(T_{B\_on} - T_{W\_on})_{\text{RRT}}$  (Figs. 6(a)–(e)).

To parameterise the radiation measurement formula,  $(T_{B\_on} - T_{W\_on})$  of the UAS is fitted with empirical equations as follows:

$$(T_{B\_on} - T_{W\_on})_{\text{UAS}} = T_0(T_{W\_on}) + A_0(T_{W\_on}) \cdot \exp(-P/P_0(T_{W\_on})) + A_1(T_{W\_on}) \cdot \exp(-P/P_1(T_{W\_on})), S_0 = 960 \text{ W} \cdot \text{m}^{-2}, \quad (2)$$

185 where  $T_0(T_{W\_on})$ ,  $A_0(T_{W\_on})$ ,  $P_0(T_{W\_on})$ ,  $A_1(T_{W\_on})$  and  $P_1(T_{W\_on})$  are the fitting coefficients with a  $T_{W\_on}$  function and units of °C, °C, hPa, °C and hPa, respectively. The dashed lines in Figs. 6(a)–(e) represent the fittings.

Interestingly,  $(T_{B\_on} - T_{W\_on})$  gradually increases with decreasing sensor temperature in the UAS. A similar phenomenon was previously observed in a chamber with no apparent air ventilation (Lee et al., 2018a). A possible reason might be that the long-wave radiation from thermistors decreases with the environmental temperature even though the irradiance is maintained at cold temperatures. To incorporate the effect of temperature ( $T_{W\_on}$ ) in Eq. (2), its coefficients of  $T_0(T_{W\_on})$ ,  $A_0(T_{W\_on})$ ,  $P_0(T_{W\_on})$ ,  $A_1(T_{W\_on})$  and  $P_1(T_{W\_on})$  are fitted with linear functions of  $T_{W\_on}$  as follows:

$$T_0(T_{W\_on}) = a_0 \cdot T_{W\_on} + a_1, \quad (3)$$

$$A_0(T_{W\_on}) = b_0 \cdot T_{W\_on} + b_1, \quad (4)$$

$$P_0(T_{W\_on}) = c_0 \cdot T_{W\_on} + c_1, \quad (5)$$

$$200 \quad A_1(T_{W\_on}) = d_0 \cdot T_{W\_on} + d_1, \quad (6)$$

$$P_1(T_{W\_on}) = e_0 \cdot T_{W\_on} + e_1, \quad (7)$$

where  $a_0$ ,  $a_1$ ,  $b_0$ ,  $b_1$ ,  $c_0$ ,  $c_1$ ,  $d_0$ ,  $d_1$ ,  $e_0$  and  $e_1$  are the fitting coefficients. These coefficients are collected from five pairs of thermistors and each coefficient is again functionalised with  $(T_{B\_on} - T_{W\_on})_{\text{RRT}}$  to incorporate the individuality of thermistors observed in RRT into Eq. (2) as follows:

$$205 \quad \text{Coefficient}_{\text{Rad\_meas}} = \text{Slope}_{\text{Rad\_meas}} \cdot (T_{B\_on} - T_{W\_on})_{\text{RRT}} + \text{Intercept}_{\text{Rad\_meas}}, \quad (8)$$

where  $\text{Coefficient}_{\text{Rad\_meas}}$  represents  $a_0$ ,  $a_1$ ,  $b_0$ ,  $b_1$ ,  $c_0$ ,  $c_1$ ,  $d_0$ ,  $d_1$ ,  $e_0$  and  $e_1$  from the five pairs of dual thermistors, and  $\text{Slope}_{\text{Rad\_meas}}$  and  $\text{Intercept}_{\text{Rad\_meas}}$  are the corresponding fitting coefficients. **Table 1** presents the  $\text{Slope}_{\text{Rad\_meas}}$  and  $\text{Intercept}_{\text{Rad\_meas}}$  values.

**Table 1.**  $\text{Slope}_{\text{Rad\_meas}}$  and  $\text{Intercept}_{\text{Rad\_meas}}$  of  $a_0$ ,  $a_1$ ,  $b_0$ ,  $b_1$ ,  $c_0$ ,  $c_1$ ,  $d_0$ ,  $d_1$ ,  $e_0$  and  $e_1$ .

Coefficient <sub>Rad_meas</sub>	Unit	Slope <sub>Rad_meas</sub>	Intercept <sub>Rad_meas</sub>
---------------------------------	------	---------------------------	-------------------------------



$a_0$		0	$2.7 \times 10^{-1}$
$a_1$	°C	0	$3.3 \times 10^{-1}$
$b_0$		$-8.8 \times 10^{-4}$	$4.8 \times 10^{-1}$
$b_1$	°C	$-1.0 \times 10^{-3}$	$6.3 \times 10^{-2}$
$c_0$	hPa·°C <sup>-1</sup>	$1.4 \times 10^{-2}$	$-3.1 \times 10^{-1}$
$c_1$	hPa	$6.6 \times 10^{-3}$	17.8
$d_0$		$-3.5 \times 10^{-4}$	$4.3 \times 10^{-1}$
$d_1$	°C	$-1.5 \times 10^{-3}$	$7.8 \times 10^{-2}$
$e_0$	hPa·°C <sup>-1</sup>	$-2.8 \times 10^{-1}$	-6.4
$e_1$	hPa	$2.1 \times 10^{-1}$	235.8

210

During sounding, the irradiance ( $S$ ) is unknown but can be found using  $(T_B - T_W)$  of DTR. Hence, Eq. (2) is employed to measure the *in-situ* irradiance based on the fact that  $(T_{B\_on} - T_{W\_on})_{UAS}$  is linearly proportional to  $S$  (Lee et al., 2018a; Lee et al., 2018b):

$$S = S_0 \times (T_{B\_on} - T_{W\_on})_{UAS} / [T_0(T_{W\_on}) + A_0(T_{W\_on}) \cdot \exp(-P/P_0(T_{W\_on})) + A_1(T_{W\_on}) \cdot \exp(-P/P_1(T_{W\_on}))], S_0 = 960 \text{ W} \cdot \text{m}^{-2}, \quad (9)$$

215 where the result of individual radiation test  $(T_{B\_on} - T_{W\_on})_{RRT}$  is incorporated using Eqs. (3)–(8). Consequently, Fig. 6(f) shows the fitting residual by Eq. (9) to estimate the irradiance ( $960 \text{ W} \cdot \text{m}^{-2}$ ) by using  $(T_{B\_on} - T_{W\_on})_{UAS}$ ,  $(T_{B\_on} - T_{W\_on})_{RRT}$  and other environmental parameters. Although the temperature difference of the five pairs of thermistors is different by nearly a factor of three, as shown in Figs. 6(a)–(e), the residuals are within  $\pm 20\%$  due to the parameterisation of the RRT value into Eq. (9).

220 In Eq. (9), the air ventilation speed ( $v$ ) imitating the ascent speed of radiosondes is fixed at  $v_0 = 5 \text{ m} \cdot \text{s}^{-1}$ . As determined,  $(T_{B\_on} - T_{W\_on})_{UAS}$  decreases by  $0.08 \text{ }^\circ\text{C}$  on average when  $v$  increases by  $1 \text{ m} \cdot \text{s}^{-1}$  due to the convective cooling in the range of  $v = 4\text{--}6.5 \text{ m} \cdot \text{s}^{-1}$  and  $P = 7\text{--}100 \text{ hPa}$  (data not shown). Thus, Eq. (9) can be revised to include the effect of air ventilation speed as follows:

$$S = S_0 \times (T_{B\_on} - T_{W\_on})_{UAS} / [T_0(T_{W\_on}) + A_0(T_{W\_on}) \cdot \exp(-P/P_0(T_{W\_on})) + A_1(T_{W\_on}) \cdot \exp(-P/P_1(T_{W\_on})) - 0.08 \cdot (v - v_0)],$$

$$S_0 = 960 \text{ W} \cdot \text{m}^{-2} \text{ and } v_0 = 5 \text{ m} \cdot \text{s}^{-1} \quad (10).$$

225

Note that Eq. (10) is used for the intercomparison sounding test, as described later.

#### 4.2 Radiation correction by DTR

230 Figures 7(a)–(e) show the UAS measurements for obtaining the radiation correction values  $(T_{W\_on} - T_{W\_off})$  of the white sensors that are selected from the RRT in Fig. 5(d). The experimental condition of Fig. 7 is identical to that of Fig. 6, wherein  $P$  varies from 5 to 500 hPa and  $T_{W\_on}$  varies from  $-68$  to  $20 \text{ }^\circ\text{C}$  with a fixed  $S_0 = 960 \text{ W} \cdot \text{m}^{-2}$  and  $v_0 = 5 \text{ m} \cdot \text{s}^{-1}$ . Since





the level of  $(T_{W\_on} - T_{W\_off})_{RRT}$  is positively correlated with the degree of  $(T_{W\_on} - T_{W\_off})_{UAS}$ ,  $(T_{W\_on} - T_{W\_off})_{RRT}$  can be parameterised into a radiation correction formula based on  $(T_{W\_on} - T_{W\_off})_{UAS}$  to neutralise the difference among units.

To obtain the radiation correction formula of DTR,  $(T_{W\_on} - T_{W\_off})_{UAS}$  is fitted with empirical equations (dashed lines in Fig. 7) as follows:

$$235 \quad (T_{W\_on} - T_{W\_off})_{UAS} = T_1(T_{W\_on}) + A_2(T_{W\_on}) \cdot \exp(-P/P_2(T_{W\_on})) + A_3(T_{W\_on}) \cdot \exp(-P/P_3(T_{W\_on})), S_0 = 960 \text{ W} \cdot \text{m}^{-2}, \quad (11)$$

where  $T_1(T_{W\_on})$ ,  $A_2(T_{W\_on})$ ,  $P_2(T_{W\_on})$ ,  $A_3(T_{W\_on})$  and  $P_3(T_{W\_on})$  are the fitting coefficients as a function of  $T_{W\_on}$  with units of °C, °C, hPa, °C and hPa, respectively.

$(T_{W\_on} - T_{W\_off})_{UAS}$  gradually increases with decreasing sensor temperature ( $T_{W\_on}$ ) in UAS. This is attributed to the decrease of the long-wave radiation from thermistors at cold temperatures, despite the constant irradiation.

240 To incorporate the effect of temperature ( $T_{W\_on}$ ) in Eq. (11), the coefficients of  $T_1(T_{W\_on})$ ,  $A_2(T_{W\_on})$ ,  $P_2(T_{W\_on})$ ,  $A_3(T_{W\_on})$  and  $P_3(T_{W\_on})$  are fitted with linear functions of  $T_{W\_on}$  as follows:

$$T_1(T_{W\_on}) = f_0 \cdot T_{W\_on} + f_1, \quad (12)$$

$$A_2(T_{W\_on}) = g_0 \cdot T_{W\_on} + g_1, \quad (13)$$

$$P_2(T_{W\_on}) = h_0 \cdot T_{W\_on} + h_1, \quad (14)$$

$$245 \quad A_3(T_{W\_on}) = i_0 \cdot T_{W\_on} + i_1, \quad (15)$$

$$P_3(T_{W\_on}) = j_0 \cdot T_{W\_on} + j_1, \quad (16)$$

where  $f_0$ ,  $f_1$ ,  $g_0$ ,  $g_1$ ,  $h_0$ ,  $h_1$ ,  $i_0$ ,  $i_1$ ,  $j_0$  and  $j_1$  are the fitting coefficients. Then, these coefficients are collected from five pairs of thermistors and each coefficient is converted into a function of  $(T_{W\_on} - T_{W\_off})_{RRT}$  to incorporate the individuality of thermistors into Eq. (11):

$$250 \quad \text{Coefficient}_{\text{Rad\_cor}} = \text{Slope}_{\text{Rad\_cor}} \cdot (T_{W\_on} - T_{W\_off})_{RRT} + \text{Intercept}_{\text{Rad\_cor}}, \quad (17)$$

where  $\text{Coefficient}_{\text{Rad\_cor}}$  represents  $f_0$ ,  $f_1$ ,  $g_0$ ,  $g_1$ ,  $h_0$ ,  $h_1$ ,  $i_0$ ,  $i_1$ ,  $j_0$  and  $j_1$ , and  $\text{Slope}_{\text{Rad\_cor}}$  and  $\text{Intercept}_{\text{Rad\_cor}}$  represent the corresponding fitting coefficients. **Table 2** presents the  $\text{Slope}_{\text{Rad\_cor}}$  and the  $\text{Intercept}_{\text{Rad\_cor}}$  values.

**Table 2.**  $\text{Slope}_{\text{Rad\_cor}}$  and  $\text{Intercept}_{\text{Rad\_cor}}$  of  $f_0$ ,  $f_1$ ,  $g_0$ ,  $g_1$ ,  $h_0$ ,  $h_1$ ,  $i_0$ ,  $i_1$ ,  $j_0$  and  $j_1$ .

Coefficient <sub>Rad_cor</sub>	Unit	Slope <sub>Rad_cor</sub>	Intercept <sub>Rad_cor</sub>
$f_0$		0	$3.0 \times 10^{-1}$
$f_1$	°C	0	$-1.3 \times 10^{-1}$
$g_0$		$-2.2 \times 10^{-3}$	$4.7 \times 10^{-1}$
$g_1$	°C	$1.5 \times 10^{-3}$	$9.0 \times 10^{-2}$
$h_0$	hPa·°C <sup>-1</sup>	$-1.9 \times 10^{-2}$	$-1.7 \times 10^{-2}$
$h_1$	hPa	$3.1 \times 10^{-2}$	9.5
$i_0$		$-7.7 \times 10^{-4}$	$4.0 \times 10^{-1}$
$i_1$	°C	$-3.7 \times 10^{-4}$	$-6.4 \times 10^{-2}$



$j_0$	hPa·°C <sup>-1</sup>	$-3.1 \times 10^{-1}$	-7.0
$j_1$	hPa	$6.2 \times 10^{-1}$	135.6

255 Although the irradiance ( $S_0$ ) is fixed as  $960 \text{ W} \cdot \text{m}^{-2}$  herein,  $(T_{W\_on} - T_{W\_off})_{UAS}$  is linearly proportional to  $S$ , as experimentally and theoretically studied in previous studies (Mcmillin et al., 1992; Lee et al., 2018b). To include the irradiance ( $S$ ) obtained using Eq. (10) into the radiation correction formula, Eq. (11) is revised as follows:

$$(T_{W\_on} - T_{W\_off})_{UAS} = (S/S_0) \times [T_1(T_{W\_on}) + A_2(T_{W\_on}) \cdot \exp(-P/P_2(T_{W\_on})) + A_3(T_{W\_on}) \cdot \exp(-P/P_3(T_{W\_on}))], S_0 = 960 \text{ W} \cdot \text{m}^{-2}, \quad (18)$$

where the result of individual radiation test  $(T_{W\_on} - T_{W\_off})_{RRT}$  is incorporated using Eqs. (12)–(17).

260 The fitting residual obtained using Eq. (18) is shown in Fig. 7(f). Although the radiation correction values of the five pairs of thermistors differ by more than a factor of two, as shown in Figs. 5(a)–(e), the residuals are within  $\pm 0.2 \text{ }^\circ\text{C}$ , because the RRT results are incorporated into Eq. (18).

The air ventilation speed ( $v$ ) imitating the ascent speed of the radiosondes is fixed at  $v_0 = 5 \text{ m} \cdot \text{s}^{-1}$  in Eq. (18). As determined,  $(T_{W\_on} - T_{W\_off})_{UAS}$  decreases by  $0.1 \text{ }^\circ\text{C}$  on average when  $v$  increases by  $1 \text{ m} \cdot \text{s}^{-1}$  due to the convective cooling in the range of

265  $v = 4\text{--}6.5 \text{ m} \cdot \text{s}^{-1}$  and  $P = 7\text{--}100 \text{ hPa}$  (data not shown). Thus, Eq. (18) can be modified to include the effect of  $v$  as follows:

$$(T_{W\_on} - T_{W\_off})_{UAS} = (S/S_0) \times [T_1(T_{W\_on}) + A_2(T_{W\_on}) \cdot \exp(-P/P_2(T_{W\_on})) + A_3(T_{W\_on}) \cdot \exp(-P/P_3(T_{W\_on})) - 0.1 \cdot (v - v_0)],$$

$$S_0 = 960 \text{ W} \cdot \text{m}^{-2} \text{ and } v_0 = 5 \text{ m} \cdot \text{s}^{-1} \quad (19).$$

Note that Eq. (19) is applied to the DTR radiation correction in the intercomparison sounding test, as described later.

## 5 Sounding test of DTR

### 270 5.1 Daytime

The radiation measurement and correction formulas of the DTR obtained via laboratory characterisations were applied to the sounding test performed during July, 2021 in Jeju Island, South Korea. Figure 8(a) shows an example of the temperature difference ( $T_{B\_raw} - T_{W\_raw}$ ) between the two sensors during sounding in the daytime. Note that  $(T_{B\_raw} - T_{W\_raw})$  in the sounding data corresponds to the  $(T_{B\_on} - T_{W\_on})_{UAS}$  of the UAS experiment, and thus,  $(T_{B\_raw} - T_{W\_raw})$  is used instead of

275  $(T_{B\_on} - T_{W\_on})_{UAS}$  to obtain the irradiance using Eq. (10). Figure 8(b) displays the irradiance measured by the DTR based on the temperature difference between the dual thermistors and environmental parameters, including  $T_{W\_raw}$ ,  $P$  and  $v$ . The irradiance measured by the DTR is the effective irradiance to the thermistors including the components of direct solar irradiation, its reflection and scattering as well as the long-wave radiation from the earth. However, these components cannot be distinguished through DTR measurements. Then, using the effective irradiance ( $S$ ), the radiation correction value  $(T_{W\_raw}$

280  $- T_{W\_cor})$  of the white sensor is obtained using Eq. (19), as shown in Fig. 8(c). The correction value of the white sensor tends to gradually increase from the ground to stratosphere with some fluctuations in the troposphere due to clouds.



## 5.2 Nighttime

The radiation measurement and correction formulas of the DTR were also applied during the nighttime sounding test. Figure 8(d) shows a typical example of the temperature difference ( $T_{B\_raw} - T_{W\_raw}$ ) between dual thermistors during nighttime. Interestingly, at an altitude of 30 km, the temperature of the black sensor is lower than that of the white sensor by about 0.5 °C. This phenomenon occurs due to the high emissivity of the black sensor, which facilitates a long-wave radiation from the black sensor more than that from the white sensor. The ( $T_{B\_raw} - T_{W\_raw}$ ) converted into the effective irradiance at nighttime using Eq. (10) is negative (Fig. 8(e)). Additionally, the radiation correction value ( $T_{W\_raw} - T_{W\_cor}$ ) of the white sensor obtained using Eq. (19) is negative (Fig. 8(f)). This implies that the raw temperature of the white sensor is lower than the air temperature, and thus, the absolute correction value should be added to  $T_{W\_raw}$  for the correction.

## 6 Uncertainty evaluation and intercomparison

### 6.1 Uncertainty budget on radiation measurement by DTR

According to the radiation measurement formula by the DTR (Eq. (10)), the factors for the uncertainty of radiation measurement  $U(S)$  are  $T_{W\_on}$ ,  $P$ ,  $v$ ,  $S_0$  and fitting residuals in Fig. 6(f). These factors contribute to  $U(S)$  as follows:

$$\frac{\partial S}{\partial T_{W\_on}} \cdot U(T_{W\_on}), \quad (20)$$

$$\frac{\partial S}{\partial P} \cdot U(P), \quad (21)$$

$$\frac{\partial S}{\partial v} \cdot U(v), \quad (22)$$

$$\frac{\partial S}{\partial S_0} \cdot U(S_0), \quad (23)$$

$$\frac{S}{100} \cdot U(Fitting). \quad (24)$$

Here,  $U(\text{parameter})$  represents the expanded uncertainty of each parameter at  $k = 2$ , and the partial differential terms represent the sensitivity coefficients. The sensitivity coefficient of the uncertainty due to the fitting error  $U(Fitting)$  is  $S/100$  because it is provided as a percentage in Fig. 6(f). Then,  $U(S)$  is obtained by combining the contributions from these factors based on the uncertainty propagation law:

$$U(S) = \sqrt{\left(\frac{\partial S}{\partial T_{W\_on}}\right)^2 \cdot U(T_{W\_on})^2 + \left(\frac{\partial S}{\partial P}\right)^2 \cdot U(P)^2 + \left(\frac{\partial S}{\partial v}\right)^2 \cdot U(v)^2 + \left(\frac{\partial S}{\partial S_0}\right)^2 \cdot U(S_0)^2 + \left(\frac{S}{100}\right)^2 \cdot U(Fitting)^2} \quad (25)$$

Figures 9(a) and (b) show the average of the effective irradiance measured by DTR with the expanded uncertainty ( $k = 2$ ) calculated using Eq. (25) at daytime and nighttime, respectively. Radiation measurements by DTR from  $N = 12$  and  $N = 6$  soundings are averaged at daytime and nighttime, respectively. The negative effective irradiance at an altitude above 25 km at nighttime is statistically significant. Examples of the uncertainty budget for the radiation measurement by the DTR at an altitude of 30 km are summarised in **Table 3** and **Table 4** for daytime and nighttime, respectively.

310



**Table 3.** Daytime uncertainty budget on radiation measurement of  $S = 1141 \text{ W}\cdot\text{m}^{-2}$  by DTR at an altitude of 30 km.

Uncertainty factor	Condition at 30 km	Unit	Uncertainty ( $k = 2$ )	Contribution to uncertainty of radiation measurement ( $k = 2$ )
$T_{W\_on}$	-41.5	°C	0.23	$106 \text{ W}\cdot\text{m}^{-2}$
$P$	12.6	hPa	0.3	$5 \text{ W}\cdot\text{m}^{-2}$
$v$	6.1	$\text{m}\cdot\text{s}^{-1}$	0.12	$5 \text{ W}\cdot\text{m}^{-2}$
$S_0$	960	$\text{W}\cdot\text{m}^{-2}$	61	$73 \text{ W}\cdot\text{m}^{-2}$
Fitting error	-	%	23.4	$268 \text{ W}\cdot\text{m}^{-2}$
$U(S)$ , Expanded uncertainty for radiation measurement of $1141 \text{ W}\cdot\text{m}^{-2}$ ( $k = 2$ )				$297 \text{ W}\cdot\text{m}^{-2}$

**Table 4.** Nighttime uncertainty budget on radiation measurement of  $S = -198 \text{ W}\cdot\text{m}^{-2}$  by DTR at an altitude of 30 km.

Uncertainty factor	Condition at 30 km	Unit	Uncertainty ( $k = 2$ )	Contribution to uncertainty of radiation measurement ( $k = 2$ )
$T_{W\_on}$	-44.3	°C	0.24	$110 \text{ W}\cdot\text{m}^{-2}$
$P$	12.3	hPa	0.3	$1 \text{ W}\cdot\text{m}^{-2}$
$v$	6.3	$\text{m}\cdot\text{s}^{-1}$	0.12	$1 \text{ W}\cdot\text{m}^{-2}$
$S_0$	960	$\text{W}\cdot\text{m}^{-2}$	61	$12.5 \text{ W}\cdot\text{m}^{-2}$
Fitting error	-	%	23.4	$46 \text{ W}\cdot\text{m}^{-2}$
$U(S)$ , Expanded uncertainty for radiation measurement of $-198 \text{ W}\cdot\text{m}^{-2}$ ( $k = 2$ )				$120 \text{ W}\cdot\text{m}^{-2}$

### 315 6.2 Uncertainty on radiation correction by DTR

The radiation-corrected temperature ( $T_{W\_cor}$ ) of DTR is obtained by subtracting the radiation correction value calculated using Eq. (19) from the raw temperature ( $T_{W\_raw}$ ) of the white sensor:

$$T_{W\_cor} = T_{W\_raw} - (T_{W\_on} - T_{W\_off})_{UAS} \quad (26)$$

Then, the uncertainty of the corrected temperature  $U(T_{W\_cor})$  is calculated as follows:

$$320 \quad U(T_{W\_cor})^2 = U(T_{W\_raw})^2 + U(T_{W\_on} - T_{W\_off})_{UAS}^2 \quad (27)$$

where  $U(\text{parameter})$  is the expanded uncertainty ( $k = 2$ ). Additionally,  $U(T_{W\_raw})^2$  is the uncertainty of raw temperature that is related to the uncertainty due to the calibration  $U(T_{S\_cal})^2$  of thermistors in the climate chamber (Fig. 3) and the uncertainty due to the temperature effect on the radiosonde board  $U(T_{Board\_temp})^2$  (Fig. 4).  $U(T_{W\_on} - T_{W\_off})_{UAS}^2$  is the uncertainty of the radiation correction value that is obtained using Eq. (19), comprising uncertainty factors  $T_{W\_on}$ ,  $P$ ,  $v$  and  $S_0$



325 and fitting residuals. The fitting residuals include the uncertainty due to RRT  $U(T_{\text{RRT}})^2$  (Fig. 7). Consequently, the expanded uncertainty of the corrected temperature of the DTR is as follows:

$$U(T_{W\_cor}) = \sqrt{\left(\frac{\partial T_{W\_cor}}{\partial T_{W\_on}}\right)^2 \cdot U(T_{W\_on})^2 + \left(\frac{\partial T_{W\_cor}}{\partial P}\right)^2 \cdot U(P)^2 + \left(\frac{\partial T_{W\_cor}}{\partial v}\right)^2 \cdot U(v)^2 + \left(\frac{\partial T_{W\_cor}}{\partial S_0}\right)^2 \cdot U(S_0)^2 + 1^2 \cdot U(T_{\text{RRT}})^2 + 1^2 \cdot U(T_{S\_cal})^2 + 1^2 \cdot U(T_{\text{Board\_temp}})^2} \quad (28)$$

Figures 9(c) and (d) show  $U(T_{W\_cor})$  and its uncertainty components at daytime and nighttime, respectively. At daytime, the DTR uncertainty gradually increases up to about 0.35 °C in the troposphere and is maintained in the stratosphere. However, at nighttime, the uncertainty slightly is decreased to about 0.3 °C as the uncertainty of effective irradiance is decreased. Examples of the uncertainty budget on the radiation-corrected temperature of the DTR ( $T_{W\_cor}$ ) at an altitude of 30 km are summarised in **Table 5** and **Table 6** for daytime and nighttime, respectively.

**Table 5.** Uncertainty budget on radiation-corrected temperature by DTR at daytime at an altitude of 30 km.

Uncertainty factor	Condition at 30 km	Unit	Uncertainty ( $k = 2$ )	Contribution to uncertainty of radiation-corrected temperature ( $k = 2$ )
$T_{W\_on}$	-41.5	°C	0.23	0.000 °C
$P$	12.6	hPa	0.3	0.004 °C
$v$	6.1	$\text{m}\cdot\text{s}^{-1}$	0.12	0.01 °C
$S_0$	960	$\text{W}\cdot\text{m}^{-2}$	61	0.06 °C
Fitting error (or $T_{\text{RRT}}$ )	-	°C	0.216	0.23 °C
$T_{S\_cal}$	-41.5	°C	0.227	0.23 °C
$T_{\text{Board\_temp}}$	-41.5	°C	0.08	0.08 °C
$U(T_{W\_cor})$ , Expanded uncertainty for radiation-corrected temperature ( $k = 2$ )				0.33 °C

335

**Table 6.** Uncertainty budget on radiation-corrected temperature by DTR at nighttime at an altitude of 30 km.

Uncertainty factor	Condition at 30 km	Unit	Uncertainty ( $k = 2$ )	Contribution to uncertainty of radiation-corrected temperature ( $k = 2$ )
$T_{W\_on}$	-44.3	°C	0.24	0.000 °C
$P$	12.3	hPa	0.3	0.001 °C
$v$	6.3	$\text{m}\cdot\text{s}^{-1}$	0.12	0.002 °C
$S_0$	960	$\text{W}\cdot\text{m}^{-2}$	61	0.01 °C
Fitting error (or $T_{\text{RRT}}$ )	-	°C	0.216	0.04 °C
$T_{S\_cal}$	-44.3	°C	0.227	0.24 °C
$T_{\text{Board\_temp}}$	-44.3	°C	0.08	0.08 °C



$U(T_{W\_cor})$ , Expanded uncertainty for radiation-corrected temperature ( $k = 2$ )	0.25 °C
--	---------

Altitude-dependent  $U(T_{W\_cor})$  of DTR ( $k = 2$ ) at both daytime and nighttime is summarised in **Table 7**. The uncertainty at the tropopause (~15 km) is higher than other regions mainly because the calibration uncertainty of the thermistors increases as the temperature is lowered (Fig. 3(e)). This means that a reduction of the calibration uncertainty of massive amount of thermistors is needed to enhance the uncertainty of radiation-corrected temperature of the DTR.

**Table 7.**  $U(T_{W\_cor})$  of DTR ( $k = 2$ ) at daytime and nighttime.

Altitude	$U(T_{W\_cor}) / T_{W\_cor}$ at daytime	$U(T_{W\_cor}) / T_{W\_cor}$ at nighttime
0 km	0.14 °C / 24.6 °C	0.14 °C / 22.8 °C
5 km	0.17 °C / 0.1 °C	0.15 °C / 0.4 °C
10 km	0.24 °C / -29.3 °C	0.22 °C / -32.0 °C
15 km	0.34 °C / -68.0 °C	0.31 °C / -66.8 °C
20 km	0.35 °C / -63.2 °C	0.30 °C / -62.5 °C
25 km	0.34 °C / -50.8 °C	0.27 °C / -51.5 °C
30 km	0.33 °C / -42.5 °C	0.25 °C / -44.1 °C

### 6.3 Intercomparison of DTR with Vaisala RS41

The radiation-corrected temperature of DTR ( $T_{W\_cor} = T_{DTR}$ ) is compared to that of a commercial radiosonde (Vaisala, RS41) via dual sounding. Figures 9(e) and (f) display the difference between the DTR and RS41 temperatures ( $T_{DTR} - T_{RS41}$ ) with the DTR uncertainty ( $k = 2$ ) as error bars during the daytime and nighttime, respectively. Generally, the two temperatures are within the DTR uncertainty during both daytime and nighttime. However, the difference at daytime gradually increases with height above 15 km and becomes greater than the DTR uncertainty at 30 km. This implies that the radiation-corrected temperature of DTR is slightly higher than that of RS41 on average at daytime; however, the uncertainty of the RS41 radiosonde is not considered here. A similar trend was observed during the radiation correction of the RS41 radiosonde by GRUAN using the SISTER setup (Von Rohden et al., 2021). The radiation-correction temperature of the RS41 radiosonde obtained by GRUAN is higher than that provided by Vaisala at daytime.

### 7 Conclusions

The performance and uncertainty of DTR were evaluated via a series of laboratory setups and intercomparison sounding with a commercial radiosonde (Vaisala, RS41). The DTR comprises two temperature sensors (white and black) with different emissivities; their temperature difference can be used for the *in-situ* measurement of the effective irradiance and the



correction of the radiation-induced bias of the white sensor. The thermistors were individually calibrated in the range of  
–70–30 °C in a climate chamber, and the uncertainty due to the calibration was evaluated. Moreover, the effect of  
360 temperature on resistance reading by radiosonde boards was investigated from –70 to 20 °C in the climate chamber, and the  
corresponding uncertainty was evaluated. RRT was individually performed on the thermistors to compensate for the unit  
difference. Parameterisation of the radiation measurements and correction formulas of DTR was performed via UAS  
experiments with varying temperature, pressure and ventilation speed. The fitting residual of the five DTRs selected from  
RRT was within 0.2 °C. The radiation measurement and correction formulas obtained by UAS were applied to the sounding  
365 test of DTR conducted in July, 2021. The method of obtaining the radiation-correction value of DTR using the effective  
irradiance measured by the temperature difference between dual sensors during sounding was demonstrated. Then, the  
contributing uncertainty factors on the corrected temperature of DTR were summarised for both daytime and nighttime.  
Generally, the uncertainty of the radiation-corrected temperature of DTR was about 0.35 °C at daytime and 0.3 °C at  
nighttime with the coverage factor  $k = 2$ . The corrected temperature of DTR was mostly consistent with that of RS41 within  
370 the expanded DTR uncertainty. The DTR methodology aims at enhancing the accuracy of the temperature measurement in  
the upper air based on *in-situ* radiation measurements. Future works may include more sounding tests in various conditions  
including cloudy and windy weather to better characterise the DTR performance of *in-situ* radiation measurements and  
corrections. Moreover, an extension of the environmental ranges, such as temperature and pressure, is desirable to cover the  
upper air environments of global areas.

#### 375 *Acknowledgement*

This work was supported by the Korea Research Institute of Standards and Science (Grant no. GP2021-0005-02).

#### *Author contribution*

SL analysed the experimental data and wrote the manuscript. SK, YL, JY and JS conducted the experiments. CB revised the  
experimental setup. SL and SK developed the measurement software. YK designed the experiments.

#### 380 *Competing interests*

The authors declare that they have no conflicts of interest.



## References

- 385 Bojinski, S., Verstraete, M., Peterson, T. C., Richter, C., Simmons, A., and Zemp, M.: The concept of essential climate variables in support of climate research, applications, and policy, *Bulletin of the American Meteorological Society*, 95, 1431-1443, <https://doi.org/10.1175/BAMS-D-13-00047.1>, 2014.
- Cuccaro, R., Rosso, L., Smorgon, D., Beltramo, G., Tabandeh, S., and Fericola, V.: Development of a low frost-point generator operating at sub-atmospheric pressure, *Measurement Science and Technology*, 29, 054002, [10.1088/1361-6501/aaa785](https://doi.org/10.1088/1361-6501/aaa785), 2018.
- 390 Dirksen, R., Sommer, M., Immler, F., Hurst, D., Kivi, R., and Vömel, H.: Reference quality upper-air measurements: GRUAN data processing for the Vaisala RS92 radiosonde, *Atmospheric Measurement Techniques*, 7, 4463-4490, <https://doi.org/10.5194/amt-7-4463-2014>, 2014.
- GCOS: GCOS Reference Upper-Air Network (GRUAN): Justification, requirements, siting and instrumentation options, Available at: [https://library.wmo.int/doc\\_num.php?explnum\\_id=3821](https://library.wmo.int/doc_num.php?explnum_id=3821) [Accessed 5th August 2021], 2007.
- 395 Key, J. R. and Schweiger, A. J.: Tools for atmospheric radiative transfer: Streamer and FluxNet, *Computers & Geosciences*, 24, 443-451, [https://doi.org/10.1016/S0098-3004\(97\)00130-1](https://doi.org/10.1016/S0098-3004(97)00130-1), 1998.
- Lee, S.-W., Kim, S., Lee, Y.-S., Choi, B. I., Kang, W., Oh, Y. K., Park, S., Yoo, J.-K., Lee, J., Lee, S., Kwon, S., and Kim, Y.-G.: Radiation correction and uncertainty evaluation of RS41 temperature sensors by using an upper-air simulator, *Atmos. Meas. Tech. Discuss.* [preprint], <https://doi.org/10.5194/amt-2021-246>, in review, 2021.
- 400 Lee, S. W., Park, E. U., Choi, B. I., Kim, J. C., Woo, S. B., Park, S., Yang, S. G., and Kim, Y. G.: Dual temperature sensors with different emissivities in radiosondes for the compensation of solar irradiation effects with varying air pressure, *Meteorological Applications*, 25, 49-55, <https://doi.org/10.1002/met.1668>, 2018a.
- Lee, S. W., Park, E. U., Choi, B. I., Kim, J. C., Woo, S. B., Kang, W., Park, S., Yang, S. G., and Kim, Y. G.: Compensation of solar radiation and ventilation effects on the temperature measurement of radiosondes using dual thermistors, *Meteorological Applications*, 25, 209-216, <https://doi.org/10.1002/met.1683>, 2018b.
- 405 Lee, S. W., Yang, I., Choi, B. I., Kim, S., Woo, S. B., Kang, W., Oh, Y. K., Park, S., Yoo, J. K., and Kim, J. C.: Development of upper air simulator for the calibration of solar radiation effects on radiosonde temperature sensors, *Meteorological Applications*, 27, e1855, <https://doi.org/10.1002/met.1855>, 2020.
- Luers, J. K.: Estimating the temperature error of the radiosonde rod thermistor under different environments, *Journal of Atmospheric and Oceanic Technology*, 7, 882-895, [https://doi.org/10.1175/1520-0426\(1990\)007<0882:ETTEOT>2.0.CO;2](https://doi.org/10.1175/1520-0426(1990)007<0882:ETTEOT>2.0.CO;2), 1990.
- McMillin, L., Uddstrom, M., and Coletti, A.: A procedure for correcting radiosonde reports for radiation errors, *Journal of Atmospheric and Oceanic Technology*, 9, 801-811, [https://doi.org/10.1175/1520-0426\(1992\)009<0801:APFCRR>2.0.CO;2](https://doi.org/10.1175/1520-0426(1992)009<0801:APFCRR>2.0.CO;2), 1992.





- 415 Merlone, A., Lopardo, G., Sanna, F., Bell, S., Benyon, R., Bergerud, R. A., Bertiglia, F., Bojkovski, J., Böse, N., and Brunet, M.: The MeteoMet project—metrology for meteorology: challenges and results, *Meteorological Applications*, 22, 820-829, <https://doi.org/10.1002/met.1528>, 2015.
- Merlone, A., Sanna, F., Beges, G., Bell, S., Beltramo, G., Bojkovski, J., Brunet, M., Del Campo, D., Castrillo, A., and Chiodo, N.: The MeteoMet2 project—highlights and results, *Measurement Science and Technology*, 29, 025802, [10.1088/1361-6501/aa99fc](https://doi.org/10.1088/1361-6501/aa99fc), 2018.
- Nash, J., Oakley, T., Vömel, H., and Li, W.: WMO intercomparisons of high quality radiosonde systems., WMO/TD-1580, Available at: [https://library.wmo.int/doc\\_num.php?explnum\\_id=9467](https://library.wmo.int/doc_num.php?explnum_id=9467), 2011.
- Philipona, R., Kräuchi, A., Romanens, G., Levrat, G., Ruppert, P., Brocard, E., Jeannet, P., Ruffieux, D., and Calpini, B.: Solar and thermal radiation errors on upper-air radiosonde temperature measurements, *Journal of Atmospheric and Oceanic Technology*, 30, 2382-2393, <https://doi.org/10.1175/JTECH-D-13-00047.1>, 2013.
- Sairanen, H., Heinonen, M., and Högström, R.: Validation of a calibration set-up for radiosondes to fulfil GRUAN requirements, *Measurement Science and Technology*, 26, 105901, <https://doi.org/10.1088/0957-0233/26/10/105901>, 2015.
- von Rohden, C., Sommer, M., Naebert, T., Motuz, V., and Dirksen, R. J.: Laboratory characterisation of the radiation temperature error of radiosondes and its application to the GRUAN data processing for the Vaisala RS41, *Atmos. Meas. Tech. Discuss.* [preprint], <https://doi.org/10.5194/amt-2021-187>, in review, 2021.
- 430 White, D.: Interpolation errors in thermistor calibration equations, *International Journal of Thermophysics*, 38, 59, [10.1007/s10765-017-2194-x](https://doi.org/10.1007/s10765-017-2194-x), 2017.



435 **Figure captions**

**Figure 1.** (a) Dual thermistor radiosonde (DTR) with a white and black sensor and (b) operation principle of DTR for irradiance measurement and correction of radiation effect based on the measured irradiance.

**Figure 2.** Characterisations of DTR. (a) Individual calibration of thermistors in a climate chamber, (b) test of the effect of temperature on the resistance reading using the radiosonde boards in the climate chamber, (c) radiation test on individual  
440 thermistors, (d) parameterisation of radiation measurement and correction formulae using an upper air simulator and (e) sounding test by applying laboratory characterisation results.

**Figure 3.** Calibration of individual thermistors in a climate chamber. (a) Calibration setup showing thermistors on booms (left), a digital multimeter to read the sensor resistance (top-right) and a data acquisition computer (bottom-right). (b) Maximum temperature gradient ( $T_{\text{Ref\_grad}}$ ) with respect to the average of five reference thermometers ( $T_{\text{Ref\_aver}}$ ) as a function  
445 of  $T_{\text{Ref\_aver}}$ . Distribution of the residuals of the (c) white and (d) black sensors by individually applying the calibration curves. (e) The uncertainty budget on the radiosonde thermistor calibration,  $U(T_{\text{S\_cal}})$ , with a coverage factor  $k = 2$ . Uncertainty factors including reference temperature gradient  $U(T_{\text{Ref\_grad}})$ , stability  $U(T_{\text{Ref\_stab}})$  and calibration  $U(T_{\text{Ref\_cal}})$ , radiosonde sensor stability  $U(T_{\text{S\_stab}})$  and fitting residual  $U(T_{\text{S\_fit\_resid}})$  are considered for  $U(T_{\text{S\_cal}})$ .

**Figure 4.** Test of the temperature effect on resistance reading by radiosonde boards. (a) Test setup showing the radiosonde  
450 boards in a climate chamber (left), reference resistors (top-right) and a data acquisition computer (bottom-right). (b) Difference between the reference resistance and radiosonde reading as a function of the reference resistance. (c) Residual represented by °C as a function of temperature when resistance is converted into temperature.

**Figure 5.** Rotational radiation test (RRT) on radiosonde thermistors individually. (a) RRT setup showing the radiosonde thermistors in a chamber, solar simulator, and vacuum pump (left), a digital multimeter (top-right) and a data acquisition  
455 computer (bottom-right). (b) Temperature measured by a white ( $T_{\text{W}}$ ) and black ( $T_{\text{B}}$ ) sensor with/without light irradiation by the solar simulator. (c) Distribution of the temperature difference between the paired white and black sensors. (d) Distribution of the temperature increase of white sensors by the irradiation. Five pairs of a white and black sensor were selected for radiation correction experiments using an upper air simulator (UAS), as indicated by black arrows in c and d.

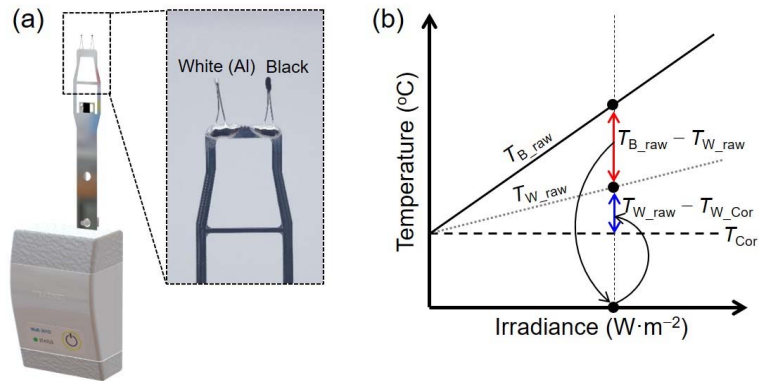
**Figure 6.** Temperature difference between paired white and black sensors ( $T_{\text{B\_on}} - T_{\text{W\_on}}$ ) investigated using UAS. (a–e)  
460 ( $T_{\text{B\_on}} - T_{\text{W\_on}}$ ) of the five paired radiosonde thermistors as a function of air pressure with varying temperature. (f) Residual of irradiance calculated on the basis of ( $T_{\text{B\_on}} - T_{\text{W\_on}}$ ) obtained in UAS and the rotational radiation test.

**Figure 7.** Radiation correction value of white sensors ( $T_{\text{W\_on}} - T_{\text{W\_off}}$ ) investigated using UAS. (a–e) ( $T_{\text{W\_on}} - T_{\text{W\_off}}$ ) of the five radiosonde white sensors as a function of air pressure with varying temperature. (f) Residual of correction value calculated on the basis of ( $T_{\text{W\_on}} - T_{\text{W\_off}}$ ) in UAS and the rotational radiation test.

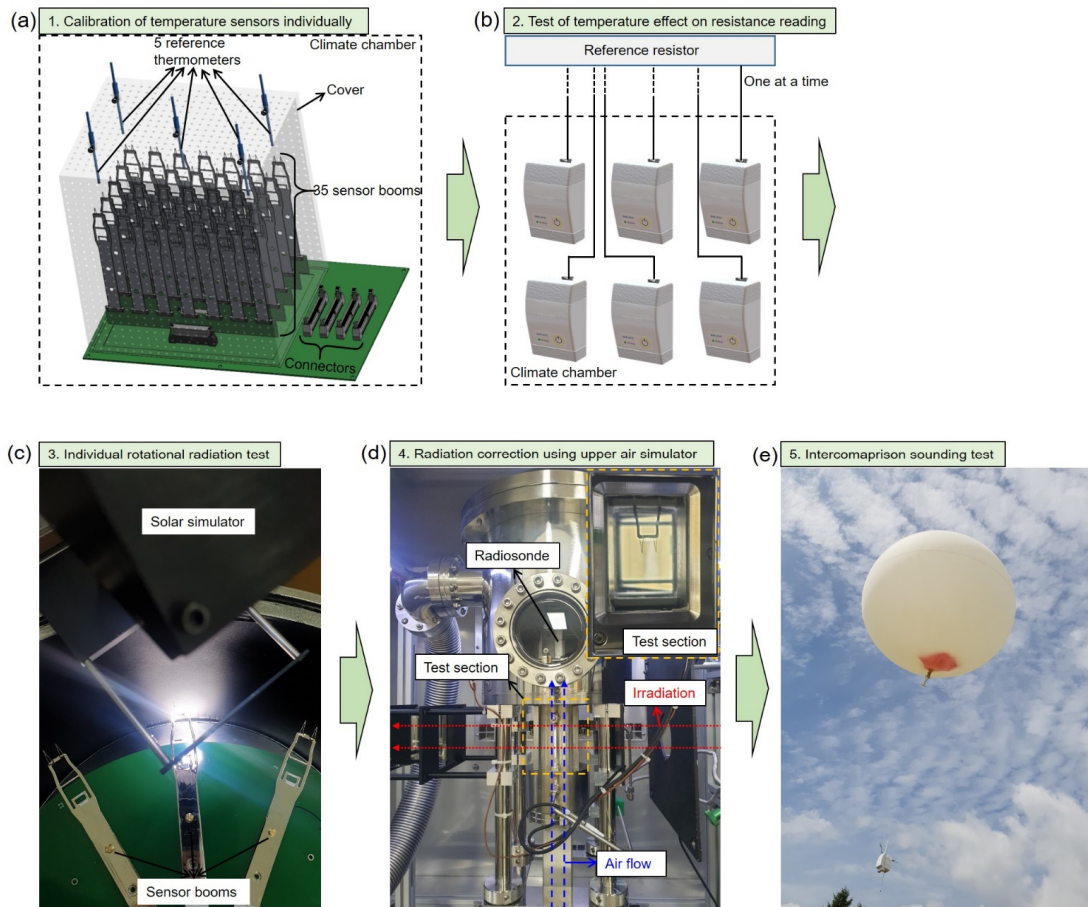


465 **Figure 8.** Sounding test of dual thermistor radiosondes. (a) Raw temperature difference between the white and black sensors ( $T_{B\_raw} - T_{W\_raw}$ ), (b) calculated effective irradiance based on ( $T_{B\_raw} - T_{W\_raw}$ ) and (c) radiation correction value of the white sensor at daytime. (d) Raw temperature difference between the white and black sensors ( $T_{B\_raw} - T_{W\_raw}$ ), (e) calculated effective irradiance ( $T_{B\_raw} - T_{W\_raw}$ ) and (f) radiation correction value of the white sensor at nighttime.

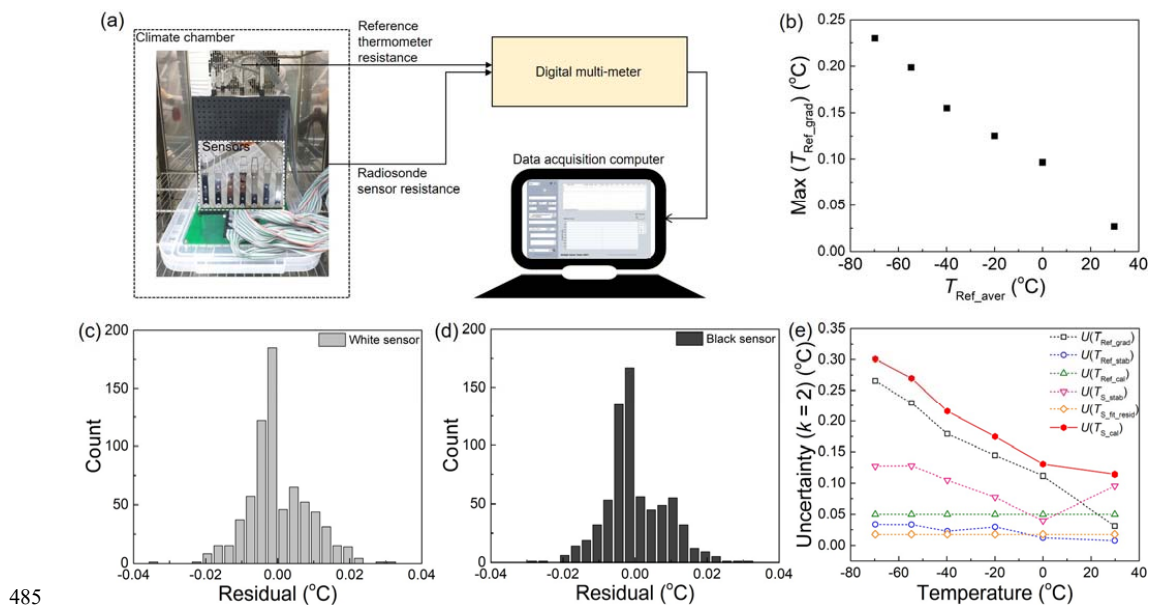
470 **Figure 9.** Uncertainty analysis on the DTR and intercomparison with Vaisala RS41. (a) Daytime and (b) nighttime effective irradiance measured by DTR with uncertainty ( $k = 2$ ). Uncertainty factors contributing to the uncertainty of the corrected temperature  $U(T_{W\_cor})$  of DTR at (c) daytime and (d) nighttime. Temperature difference between DTR and RS41 with DTR uncertainty ( $k = 2$ ) at (e) daytime and (f) nighttime.



475 **Figure 1.** (a) Dual thermistor radiosonde (DTR) with a white and black sensor and (b) operation principle of DTR for irradiance measurement and correction of radiation effect based on the measured irradiance.



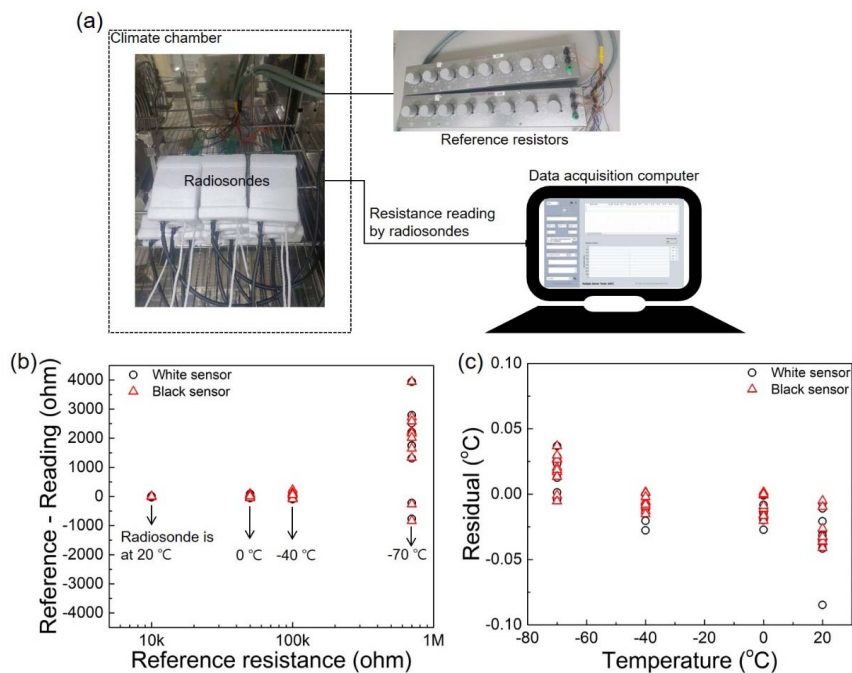
480 **Figure 2.** Characterisations of DTR. (a) Individual calibration of thermistors in a climate chamber, (b) test of the effect of temperature on the resistance reading using the radiosonde boards in the climate chamber, (c) radiation test on individual thermistors, (d) parameterisation of radiation measurement and correction formulae using an upper air simulator and (e) sounding test by applying laboratory characterisation results.



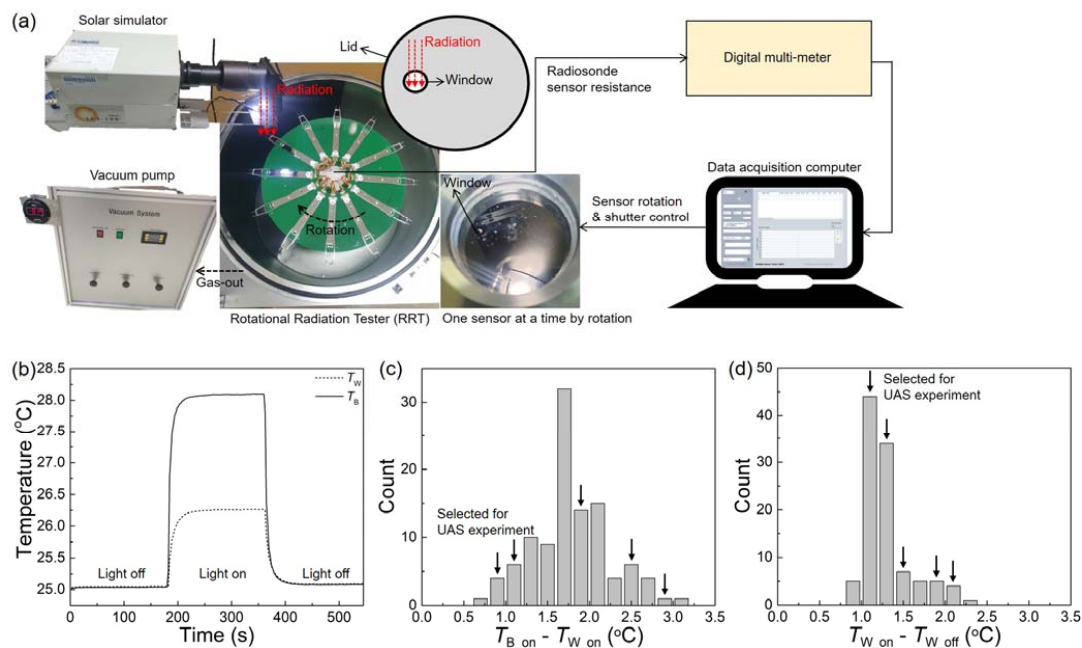
485

490

**Figure 3.** Calibration of individual thermistors in a climate chamber. (a) Calibration setup showing thermistors on booms (left), a digital multimeter to read the sensor resistance (top-right) and a data acquisition computer (bottom-right). (b) Maximum temperature gradient ( $T_{\text{Ref\_grad}}$ ) with respect to the average of five reference thermometers ( $T_{\text{Ref\_aver}}$ ) as a function of  $T_{\text{Ref\_aver}}$ . Distribution of the residuals of the (c) white and (d) black sensors by individually applying the calibration curves. (e) The uncertainty budget on the radiosonde thermistor calibration,  $U(T_{\text{S\_cal}})$ , with a coverage factor  $k = 2$ . Uncertainty factors including reference temperature gradient  $U(T_{\text{Ref\_grad}})$ , stability  $U(T_{\text{Ref\_stab}})$  and calibration  $U(T_{\text{Ref\_cal}})$ , radiosonde sensor stability  $U(T_{\text{S\_stab}})$  and fitting residual  $U(T_{\text{fit\_resid}})$  are considered for  $U(T_{\text{S\_cal}})$ .



495 **Figure 4.** Test of the temperature effect on resistance reading by radiosonde boards. (a) Test setup showing the radiosonde boards in a climate chamber (left), reference resistors (top-right) and a data acquisition computer (bottom-right). (b) Difference between the reference resistance and radiosonde reading as a function of the reference resistance. (c) Residual represented by °C as a function of temperature when resistance is converted into temperature.



500 **Figure 5.** Rotational radiation test (RRT) on radiosonde thermistors individually. (a) RRT setup showing the radiosonde  
 thermistors in a chamber, solar simulator, and vacuum pump (left), a digital multimeter (top-right) and a data acquisition  
 computer (bottom-right). (b) Temperature measured by a white ( $T_w$ ) and black ( $T_b$ ) sensor with/without light irradiation by  
 the solar simulator. (c) Distribution of the temperature difference between the paired white and black sensors. (d)  
 Distribution of the temperature increase of white sensors by the irradiation. Five pairs of a white and black sensor were  
 505 selected for radiation correction experiments using an upper air simulator (UAS), as indicated by black arrows in c and d.



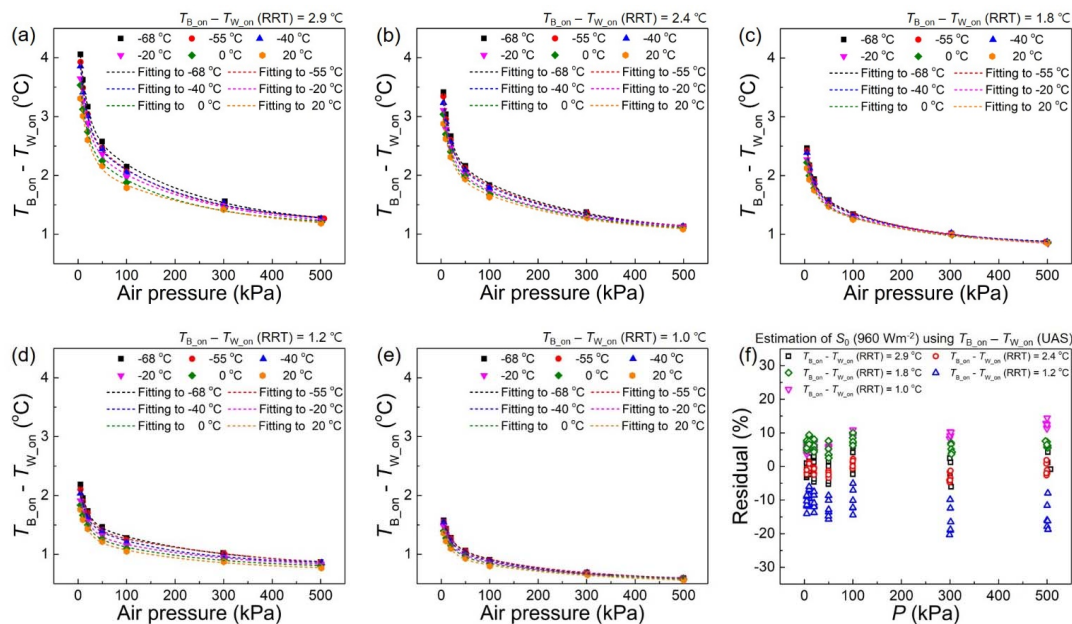


**Figure 6.** Temperature difference between paired white and black sensors ( $T_{B,on} - T_{W,on}$ ) investigated using UAS. (a–e) ( $T_{B,on} - T_{W,on}$ ) of the five paired radiosonde thermistors as a function of air pressure with varying temperature. (f) Residual of irradiance calculated on the basis of ( $T_{B,on} - T_{W,on}$ ) obtained in UAS and the rotational radiation test.

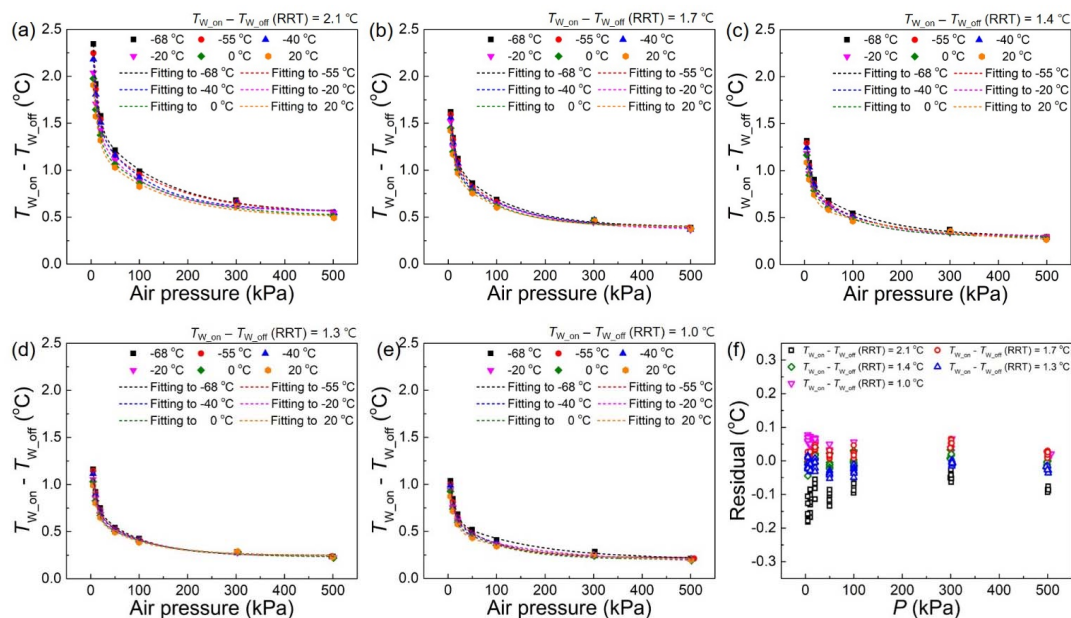


**Figure 7.** Radiation correction value of white sensors ( $T_{W\_on} - T_{W\_off}$ ) investigated using UAS. (a–e) ( $T_{W\_on} - T_{W\_off}$ ) of the five radiosonde white sensors as a function of air pressure with varying temperature. (f) Residual of correction value calculated on the basis of ( $T_{W\_on} - T_{W\_off}$ ) in UAS and the rotational radiation test.

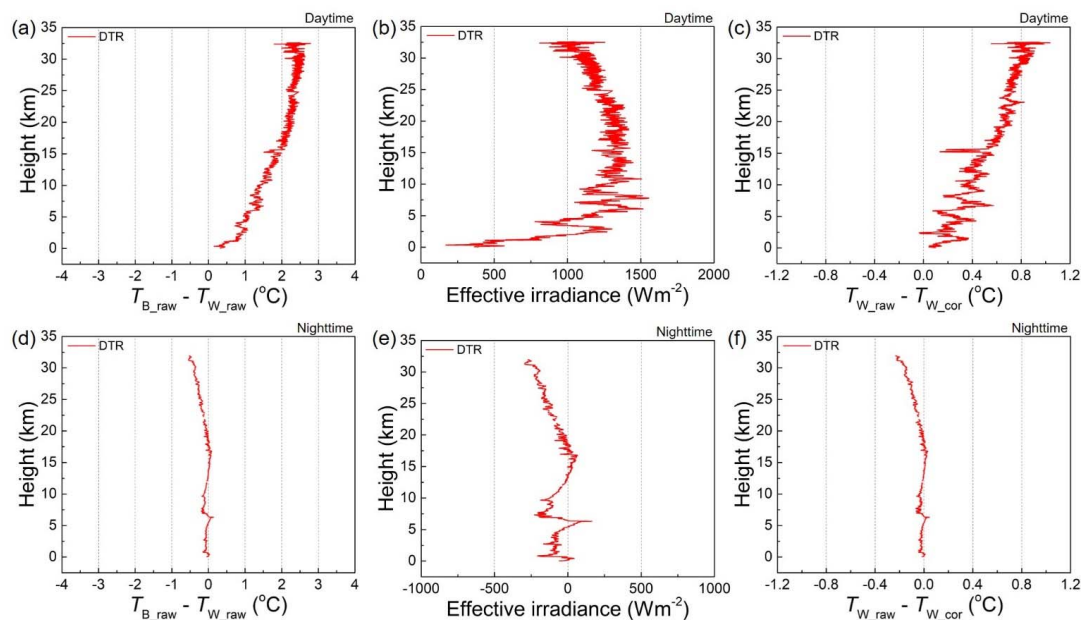


**Figure 8.** Sounding test of dual thermistor radiosondes. (a) Raw temperature difference between the white and black sensors ( $T_{B\_raw} - T_{W\_raw}$ ), (b) calculated effective irradiance based on ( $T_{B\_raw} - T_{W\_raw}$ ) and (c) radiation correction value of the white sensor at daytime. (d) Raw temperature difference between the white and black sensors ( $T_{B\_raw} - T_{W\_raw}$ ), (e) calculated effective irradiance ( $T_{B\_raw} - T_{W\_raw}$ ) and (f) radiation correction value of the white sensor at nighttime.

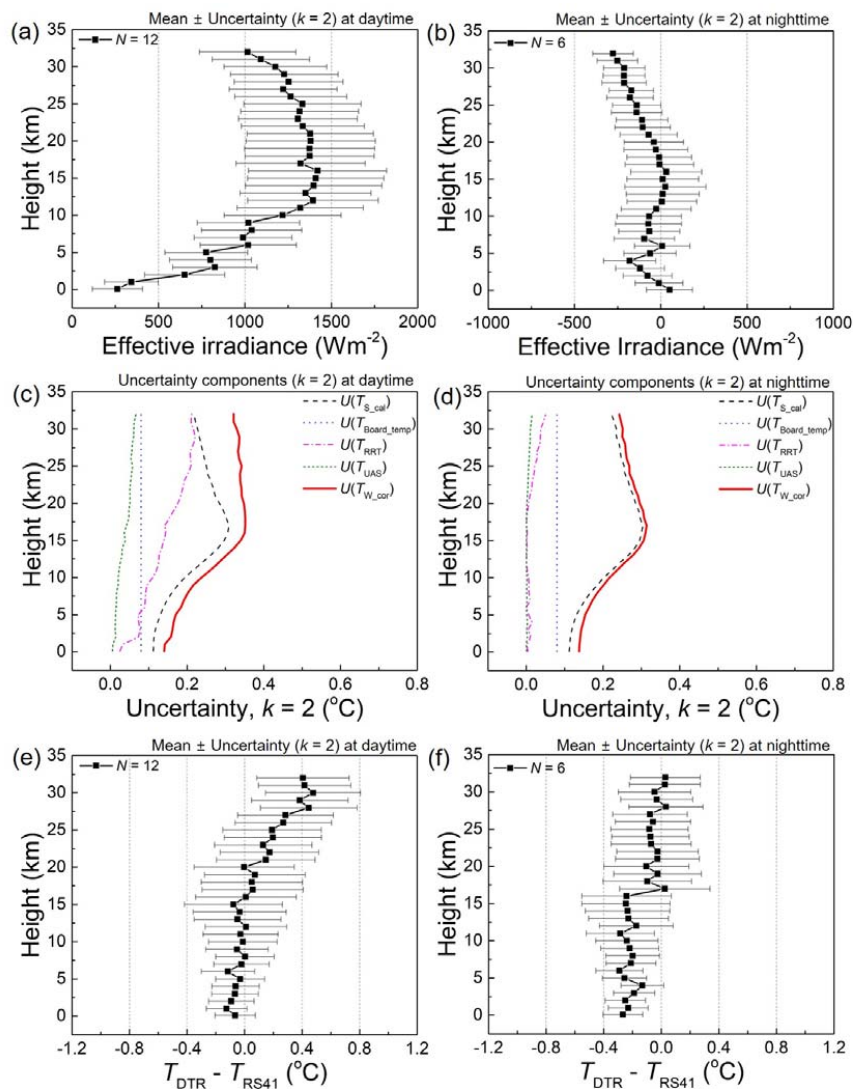


**Figure 9.** Uncertainty analysis on the DTR and intercomparison with Vaisala RS41. (a) Daytime and (b) nighttime effective irradiance measured by DTR with uncertainty ( $k = 2$ ). Uncertainty factors contributing to the uncertainty of the corrected temperature  $U(T_{W\_cor})$  of DTR at (c) daytime and (d) nighttime. Temperature difference between DTR and RS41 with DTR uncertainty ( $k = 2$ ) at (e) daytime and (f) nighttime.